














# A spatially resolved spectral analysis of giant radio galaxies with MeerKAT

K. K. L. Charlton <sup>1,★</sup>, J. Delhaize <sup>1,★</sup>, K. Thorat,<sup>2</sup> I. Heywood,<sup>3,4,5</sup> M. J. Jarvis <sup>3,6</sup>, M. J. Hardcastle <sup>7</sup>,  
F. An,<sup>8,9</sup> I. Delvecchio <sup>10</sup>, C. L. Hale <sup>3</sup>, I. H. Whittam <sup>3,6</sup>, M. Brüggén <sup>11</sup>, L. Marchetti <sup>1,12</sup>,  
L. Morabito <sup>13</sup>, Z. Randriamanakoto <sup>14,15</sup>, S. V. White <sup>5,13</sup> and A. R. Taylor <sup>1,6,16</sup>

<sup>1</sup>Department of Astronomy, University of Cape Town, Private Bag X3, Rondebosch 7701, South Africa

<sup>2</sup>Department of Physics, University of Pretoria, Private Bag X20, Hatfield 0028, South Africa

<sup>3</sup>Oxford Astrophysics, Denys Wilkinson Building, University of Oxford, Keble Road, Oxford OX1 3RH, UK

<sup>4</sup>Department of Physics and Electronics, Rhodes University, PO Box 94, Makhanda 6140, South Africa

<sup>5</sup>South African Radio Astronomy Observatory, 2 Fir Street, Black River Park, Observatory, Cape Town 7925, South Africa

<sup>6</sup>Department of Physics and Astronomy, University of the Western Cape, Robert Sobukwe Road, Bellville 7535, South Africa

<sup>7</sup>Department of Physics, Astronomy and Mathematics, University of Hertfordshire, College Lane, Hatfield AL10 9AB, UK

<sup>8</sup>Purple Mountain Observatory, Chinese Academy of Sciences, 10 Yuanhua Road, Qixia District, Nanjing 210023, China

<sup>9</sup>Department of Physics and Astronomy, University of the Western Cape, Inter-University Institute for Data Intensive Astronomy, Robert Sobukwe Road, Bellville 7535, South Africa

<sup>10</sup>INAF - Osservatorio di Astrofisica e Scienza dello Spazio di Bologna, via Gobetti 93/3, I-40129 Bologna, Italy

<sup>11</sup>Hamburger Sternwarte, University of Hamburg, Gojenbergsweg 112, D-21029 Hamburg, Germany

<sup>12</sup>INAF - Istituto di Radioastronomia, via Gobetti 101, I-40129 Bologna, Italy

<sup>13</sup>Centre for Extragalactic Astronomy, Department of Physics, Durham University, Durham DH1 3LE, UK

<sup>14</sup>South African Astronomical Observatory, PO Box 9, Observatory, Cape Town 7935, South Africa

<sup>15</sup>Department of Physics, Faculty of Sciences, University of Antananarivo, BP 906, Antananarivo 101, Madagascar

<sup>16</sup>Department of Astronomy, University of Cape Town, The Inter-University Institute for Data Intensive Astronomy (IDIA), Private Bag X3, Rondebosch 7701, South Africa

Accepted 2024 November 1. Received 2024 October 21; in original form 2024 July 11

## ABSTRACT

In this study we report the spatially resolved, wideband spectral properties of three giant radio galaxies (GRGs) in the COSMOS field: MGTC J095959.63+024608.6, MGTC J100016.84+015133.0, and MGTC J100022.85+031520.4. One of these galaxies, MGTC J100022.85+031520.4, is reported here for the first time, with a projected linear size of 1.29 Mpc at a redshift of 0.1034. Unlike the other two, it is associated with a brightest cluster galaxy (BCG), making it one of the few GRGs known to inhabit cluster environments. We examine the spectral age distributions of the three GRGs using new MeerKAT UHF-band (544–1088 MHz) observations, and *L*-band (900–1670 MHz) data from the MeerKAT International GHz Tiered Extragalactic Exploration (MIGHTEE) survey. We test two models of spectral ageing, the Jaffe–Perola and Tribble models, using the Broadband Radio Astronomy Tools (BRATS) software, and find that they agree well with each other. We estimate the Tribble spectral age for MGTC J095959.63+024608.6 as 68 Myr, for MGTC J100016.84+015133.0 as 47 Myr, and for MGTC J100022.85+031520.4 as 67 Myr. We find significant disagreements between these spectral age estimates and the estimates of the dynamical ages of these GRGs, modelled in cluster and group environments. Our results highlight the need for additional processes that are not accounted for in either the dynamic age or the spectral age estimations.

**Key words:** methods: observational – galaxies: active – galaxies: evolution – galaxies: nuclei – radio continuum: galaxies.

## 1 INTRODUCTION

Giant radio galaxies (GRGs) display jets and lobes of synchrotron-emitting plasma that extend for more than 700 kpc in projected linear length, representing the most extended population of radio galaxies (Willis, Strom & Wilson 1974; Schoenmakers et al. 2000; Dabhade, Saikia & Mahato 2023). Their extensive relativistic jets and lobes may play an important role in the evolution of their host

galaxy and surrounding environment via ‘jet-mode’ active galactic nuclei (AGN) feedback (Bower et al. 2006; Croton et al. 2006; Fabian 2012; Heckman & Best 2014). In this mode of feedback, the AGN plasma jets travel through the interstellar medium (ISM), disturbing and heating the surrounding gas. This is thought to prevent gas cooling and to stop accretion onto the supermassive black hole, halting its growth. In GRGs, because the jets are so large, this process extends further into the intergalactic and intercluster medium (IGM and ICM). Thus, GRGs could be ideal probes of the impact of AGN activity on the IGM and may provide insights into the nature of

\* E-mail: chrkat009@myuct.ac.za (KKLC); drjdelhaize@gmail.com (JD)

the environment itself (Safouris et al. 2008; Safouris et al. 2009; Malarecki et al. 2013, 2015).

The reason for the very large sizes of GRGs is still uncertain. An early suggestion was made by Mack et al. (1998) that the extended size of GRGs is due to the underdensities found within the IGM, where the speed of the plasma is not as eroded by interactions with intervening matter. However, recent studies have reported that between 4 and 10 per cent of identified GRGs reside within high-density cluster environments (Dabhade et al. 2020; Tang et al. 2020; Simonte et al. 2024). Another potential explanation for the occurrence of GRGs is that these galaxies contain abnormally powerful AGN engines that allow the jets to expand to large scales in short amounts of time (Gopal-Krishna, Wiita & Saripalli 1989). Counter to this, Komberg & Pashchenko (2009) and Hardcastle et al. (2019) found no evidence of the massive linear size of GRGs being due to particularly powerful central engines.

A more likely scenario, then, is that GRGs represent the oldest AGN systems, where the radio jets have had enough time to evolve and grow (Subrahmanyam, Saripalli & Hunstead 1996). This scenario was previously thought to be implausible because the extrapolated number densities of GRGs as of 2021 were too low: only  $\sim 820$  had been identified compared with the hundreds of thousands of reported normal radio sources (Dabhade et al. 2020). However, recent works (e.g. Delhaize et al. 2021; Simonte et al. 2024; Oei et al. 2023; Mostert et al. 2024) suggest that the actual GRG sky density is significantly higher than indicated by previous studies. These works suggest that the surface-brightness sensitivity of telescopes was actually the limiting factor, because these giants are often faint and diffuse. According to Simonte et al. (2024), who performed a large-scale study of the radio, optical, and infrared properties of GRGs compared with regular radio galaxies, age is the main factor determining a radio galaxy’s length. Given enough time for the galaxy to evolve, the other main factors in the late-stage size of a radio galaxy are the jet power, the host galaxy mass, and the large-scale environment.

If GRGs do represent the oldest AGN systems, then studying their extended structure is crucial for understanding the evolution of galaxies, their interactions, and their effect on the IGM. This is now becoming feasible, with the number of identified GRGs having increased dramatically in the last couple of years. The most notable of these increases is due to the second data release of the Low Frequency Array (LOFAR) Two-metre Sky Survey (LOTSS-DR2, Shimwell et al. 2022) and the work of Mostert et al. (2024), which have increased the total number of identified GRGs in the literature to  $\sim 12\,000$ .

Complementary to LOFAR, which operates at  $\sim 144$  MHz, the MeerKAT radio interferometer in South Africa (Jonas & MeerKAT Team 2016) is an excellent instrument for the study of GRGs at higher frequencies ( $\sim 1$  GHz). This is due to its excellent point-source sensitivity, comparative resolution capabilities to LOFAR, and excellent  $uv$  coverage. It can currently observe in three bands: the UHF (544–1088 MHz) and  $L$  (856–1670 MHz) bands, as well as the newly commissioned  $S$  (1750–3500 MHz) band.

One of the large survey projects underway with MeerKAT is the MeerKAT International GHz Tiered Extragalactic Exploration (MIGHTEE) survey (Jarvis et al. 2016). MIGHTEE is a sensitive galaxy evolution survey over  $20\text{ deg}^2$ , targeting the fields CDFS, ELAIS-S1,  $XMM$ -LSS and COSMOS in the  $L$  and  $S$  bands.  $L$ -band continuum maps of part of the  $XMM$ -LSS and COSMOS

field have already been released to the public as part of the Early Science (ES) data release (Heywood et al. 2022). These maps are confusion-limited at an rms value of  $\sim 4.5\ \mu\text{Jy beam}^{-1}$ . Two GRGs, MGTC J095959.63+024608.6 (hereafter GRG1) and MGTC J100016.84+015133.0 (hereafter GRG2), were discovered in the MIGHTEE-COSMOS field in the ES data release and presented by Delhaize et al. (2021).

In order to probe the physical processes underlying GRGs and their impact on the surrounding environment, it is necessary to measure the time-scales or ‘ages’ involved. One way to do this is by examining the radio continuum spectrum of the GRGs to determine their spectral ages. In general, the optically thin radio spectrum can be described by a power law  $S_\nu \propto \nu^{-\alpha}$ , where the slope  $\alpha$  is the spectral index. The spectral index of the radiation is dependent on the source of the radiation, the environment, the physical processes involved, and the time-scales over which they occur. At frequencies close to  $\sim 1$  GHz, the continuum emission is affected by synchrotron losses (Harwood et al. 2013), inverse Compton scattering (Blundell, Rawlings & Willott 1999), and adiabatic losses (Blundell & Rawlings 2000), although the effects of adiabatic losses are not well constrained.

If the spectrum is taken to be dominated by synchrotron emission processes, then the lifetime  $t$  of an electron is inversely proportional to its energy and the perpendicular component of the magnetic field; that is,  $t \propto (EB_\perp^2)^{-1}$ . Thus, higher-energy electrons will lose their energy at a faster rate, which results in a ‘steeper’ spectrum in regions of older plasma (e.g. Blundell & Rawlings 2000; Harwood, Hardcastle & Croston 2015). This allows an estimate of the spectral ages of the plasma, where age is defined as the time since the plasma was last injected with newly accelerated particles. Creating a spatially resolved spectral age map of a source allows us to see in detail the dynamics and evolution of the source and how it has interacted with the environment over time.

For normal-sized radio galaxies, previous studies have found that  $\alpha$  steepens with increasing linear size and that, except at high frequencies, the rest-frame spectral indices have a stronger dependence on luminosity than on redshift (Blundell et al. 1999; Dabhade et al. 2020). The spectral index is expected to steepen in the lobes away from the hotspot as electrons are accelerated at the jet termination shock. This trend is expected to extend to GRGs. Confirmation of this is an important aspect of this work, which serves as a pilot study for the spectral analysis of a larger sample of GRGs in MIGHTEE.

In this work, we combine MIGHTEE  $L$ -band data with new MeerKAT UHF-band observations to investigate the activity and history of the diffuse emission in the jets of the MIGHTEE COSMOS GRGs via the use of spectral age models. Furthermore, a newly identified third GRG found within the UHF COSMOS region is examined. In Section 2 we discuss the data processing of the multiband data, and in Sections 3 and 4.1 we discuss our analysis of our results. The conclusions of the analysis are summarized in Section 5. Throughout this paper, we assume a  $\Lambda$ CDM cosmology of  $H_0 = 67.8\text{ km s}^{-1}\text{Mpc}^{-1}$ ,  $\Omega_\Lambda = 0.692$ , and  $\Omega_M = 0.308$  (Planck Collaboration et al. 2016).

## 2 DATA

For our spectral index analysis, we make use of MeerKAT observations of the COSMOS region in three frequency ranges centred on 632, 755, and 1284 MHz. The 1.28-GHz data come from  $L$ -band continuum maps from MIGHTEE data release 1 (DR1; Hale et al.

2024). DR1 has an expanded survey area of  $\sim 4 \text{ deg}^2$  in the COSMOS region and an improved sensitivity ( $\text{rms} \sim 3.5 \mu\text{Jy beam}^{-1}$ ) compared with the ES release ( $1.6 \text{ deg}^2$ ,  $\text{rms} \sim 4.5 \mu\text{Jy beam}^{-1}$ ). Two versions of the MIGHTEE DR1 images have been released, one maximizing resolution and the other maximizing sensitivity. We use the lower-resolution, higher-sensitivity DR1 image in this work. Full details of the observations and data processing are given by Heywood et al. (2022) and Hale et al. (2024).

The 632- and 755-MHz-centred data come from UHF-band MeerKAT Open Time observations of COSMOS (ID: SCI-20210212-JD-01; PI: Delhaize), henceforth referred to as UHF-COSMOS. Details of these observations and the full-band reduction will be presented by Delhaize et al. (in preparation). In this work, we only use the lower half of the UHF band (570–816 MHz). This is to ensure the highest signal-to-noise ratio of the diffuse GRG lobe emission, because most of this emission is seen mainly in the lower part of the band. We separate the measurement set (ms) file into two equal subbands, dubbed UHF Low and UHF Mid, respectively. This provides more spectral points to improve the accuracy of spectral index fitting.

The two subbands are separated from the original ms file using the CASA task MSTRANSFORM and imaged independently using the OXKAT pipeline<sup>1</sup> (Heywood 2020) up to and including cleaning and self-calibration (2GC). Because the 2GC calibration is sufficient, it is unnecessary to apply direction-dependent calibration (3GC). The primary and secondary calibrators are J0408–6545 and J1008+0730, respectively. Images are made with WSCLEAN using a Briggs-weighting robust parameter of  $-0.5$  and a pixel size of 2 arcsec to match the resolution parameters of the MIGHTEE  $L$ -band image as closely as possible. The images are truncated at the 30 percent primary beam power level. We also apply an inner cut to the  $uv$ -plane at 87 m. This corresponds to the shortest MeerKAT baseline at the lowest  $L$ -band frequency of 856 MHz to ensure that the  $uv$  coverage is as similar as possible in each frequency band of our analysis.

The main properties of the MIGHTEE and UHF-COSMOS data are summarized in Table 1. The  $L$ - and UHF-band images are confusion-limited, with the UHF observations reaching rms noise sensitivities of approximately  $9.2$  and  $14.6 \mu\text{Jy beam}^{-1}$  for UHF Low and Mid, respectively. The beam sizes of the lower-frequency UHF images are larger ( $\sim 14$  arcsec) compared with the  $L$ -band ( $\sim 9$  arcsec).

GRG3 (see Section 3.1) is entirely within the 30 percent primary beam cut of the UHF-COSMOS images. However, only part of the source is within the MIGHTEE DR1 region owing to the smaller field of view in the  $L$  band and the conservative primary beam cut at the edges of the mosaic. We therefore re-imaged the MIGHTEE observations of a single pointing centred on  $10^{\text{h}}00^{\text{m}}28^{\text{s}}.6$ ,  $+2^{\circ}33'33''.8$  (see the appendix of Hale et al. 2024) with a primary beam cut at the 30 percent power level. The resulting image, which we will refer to as COSMOS<sub>8</sub>, fully encompasses all emission associated with GRG3. However, it has a slightly poorer sensitivity ( $\text{rms} \sim 5.1 \mu\text{Jy beam}^{-1}$ ) compared with the full mosaic because it only contains data from a single 8-h track.

## 3 RESULTS

### 3.1 Characterizing the GRGs

As mentioned in Section 1, GRG1 and GRG2 were first identified as GRGs in the MIGHTEE ES images (Delhaize et al. 2021). These galaxies had been previously classified as extended, multiple-component radio galaxies, because the core and inner parts of the jets had been detected in previous surveys (most recently the VLA at 3 GHz; Vardoulaki et al. 2015; Smolčić et al. 2017; Vardoulaki et al. 2019). However, as a result of brightness sensitivity limits, the most extended, diffuse, and faint emission of the lobes had remained undetected until the availability of MeerKAT observations, and so these objects were not identified as giants. GRG1 and GRG2 are both low-excitation radio galaxies (LERGs) hosted by red and quenched ellipticals. For further details on GRG1 and GRG2, see Delhaize et al. (2021).

We present here a third GRG in the COSMOS field for the first time. It was discovered via visual inspection in the UHF-COSMOS continuum map using a process similar to that described by Prescott et al. (2018). An optical Hyper Suprime-Cam (HSC; Aihara et al. 2018) image of the host galaxy<sup>2</sup> is shown in Fig. 1, with MIGHTEE  $L$ -band radio contours overlaid. GRG3 does not display typical Fanaroff–Riley I/II (FRI/FRII; Fanaroff & Riley 1974) radio morphology. It is centre-brightened and there is a potential hot or warm spot in the northern lobe of the galaxy. With the centre-brightening, it is more likely a plumed FRI galaxy, similar to 3C 31 (Laing et al. 2008).

The radio core is located at  $\text{RA} = 10^{\text{h}}00^{\text{m}}22^{\text{s}}.85$  and  $\text{Dec} = +03^{\circ}15'20''.4$  and coincides with the known optical galaxy SDSS J100022.85+031520.4. According to the Sloan Digital Sky Survey Data Release 13 (SDSS DR13; Albareti et al. 2017), the galaxy has a spectroscopic redshift of  $z = 0.10344 \pm 0.00002$ . Notably, it is the central galaxy and brightest cluster galaxy (BCG) in the cluster WHL J100022.9+031521 (Wen 2012), which places it amongst the 4 percent of GRGs residing in clusters according to Simonte et al. (2024). Its location at the centre of the cluster and bent morphology in the top lobe may lead it to have similar properties to wide-angle-tail (WAT) galaxies (Burns 1990). The host’s cluster is poor, with only 10  $n_{200}$  cluster members, where  $n_{200}$  is the number of cluster members that occupy a region that has a density of 200 times the critical density of the Universe. The total mass in the same region is  $M_{200} = 1.24 \times 10^{14} M_{\odot}$  (see Section 4.2). The closest cluster member is WISEA J100021.13+031511.3 (from the ALLWISE source catalogue), with a redshift of  $z = 0.1024$  and an angular separation from GRG3 of 0.45 arcmin.

Several foreground galaxies overlap with the radio contours of GRG3, as seen in Fig. 1. The northern part of the lower lobe (S1 lobe) overlaps with the star-forming galaxy UGC 05377 ( $z = 0.007175 \pm 1.33 \times 10^{-5}$ ; Schneider et al. 1990). However, the radio contours in this region are not centred on UGC 05377, implying that at least some fraction of the emission is not due to that galaxy and is likely associated with the GRG. We do not exclude this region from our analysis because spatially resolved spectral modelling is performed on a pixel-by-pixel basis, so contamination by star formation in this area will not affect our calculations along the rest of the GRG. It is assumed that the diffuse lower lobe (S2 lobe) centred at  $10^{\text{h}}00^{\text{m}}32^{\text{s}} + 3^{\circ}10'00''$  is related to GRG3 owing to the configuration of the emission. There is a potential source located

<sup>1</sup><https://github.com/IanHeywood/oxkat>

<sup>2</sup>CDS HiPS2FITS service <https://alaska.cds.unistra.fr/h>

**Table 1.** Summary of the observations used for this study. The centre of the COSMOS field is  $10^{\text{h}}00^{\text{m}}28^{\text{s}}.6, +02^{\circ}12'21''$  in the J2000 epoch, and the centre of the COSMOS<sub>8</sub> field used for GRG3 in the *L* band is  $10^{\text{h}}00^{\text{m}}28^{\text{s}}.6, +2^{\circ}33'33''.8$ . Columns: (1) band name; (2) frequency range; (3) average effective frequency of the observation; (4) spatial resolution; (5) average rms noise level of the map.

(1) Name	(2) Frequency range (MHz)	(3) $\nu_{\text{eff}}$ (MHz)	(4) Resolution (arcsec <sup>2</sup> )	(5) rms noise level ( $\mu\text{Jy beam}^{-1}$ )
MIGHTEE <i>L</i> band	900-1670	1284	$8.90 \times 8.90$	3.5
COSMOS <sub>8</sub> <i>L</i> band	900-1670	1284	$8.69 \times 6.69$	5.1
UHF Mid	693-816	755	$11.70 \times 11.70$	9.2
UHF Low	570-692	632	$14.08 \times 14.08$	14.6

at  $10^{\text{h}}00^{\text{m}}33^{\text{s}}, 3^{\circ}10'12''$ , which we assume to be a star as it is listed as such in the SDSS DR6 catalogue (Adelman-McCarthy et al. 2008), and there is no counterpart in the HSC catalogue. As with UGC 05377, we include this region in our analysis, with the caveat that it might contain contaminating emission not associated with the GRG.

With these assumptions, the total projected angular size of the radio galaxy measured between the outer edges of the northern lobe and the S2 lobe is 12.0 arcmin. This gives it a projected linear size of 1.29 Mpc, establishing it as a GRG. Even if the entirety of the southern lobe is discounted, the remaining extent between the northern lobe and the southern part of the inner jet has a projected length of slightly above 700 kpc, and the source would still be classified as a GRG. The cyan contour in Fig. 1 encompasses all emission we consider to be associated with the GRG.

The basic properties of all three GRGs found within MIGHTEE COSMOS are given in Table 2. Their total-intensity maps in the UHF-low, UHF-mid, and *L* bands are shown in Figs 2, 3, and 4. The *L*-band images and associated properties differ slightly from those in Delhaize et al. (2021), because the images have been smoothed to the same resolution as the UHF-low images, and we also use the MIGHTEE DR1 rather than the ES release. The extent of each galaxy, determining its total length, is indicated by a  $3\sigma$  flux-density contour in the *L* band, shown in cyan. The *L*-band image is used in preference to the UHF images to determine the full extent owing to its better sensitivity, revealing more of the diffuse outer lobe emission.

Table 3 presents the integrated flux densities ( $S_{\text{int}}$ ), integrated spectral indices ( $\alpha$ ), and total radio power of each GRG from the intensity maps within the defined extent. The total integrated flux density is the sum of the northern lobe, southern lobe, and core contributions to the flux density. The uncertainty of  $S_{\text{int}}$  is dominated by the  $\sim 10$  per cent uncertainty on the flux scale; however, we also combine it in quadrature with the thermal and confusion noise. A thermal noise map was created using BREIZORRO,<sup>3</sup> with a threshold of  $3\sigma$ . A confusion-noise map was created with the PYTHON Blob Detector and Source Finder (PYBDSF; Mohan & Rafferty 2015) using a pixel threshold of  $5\sigma$  and an island threshold of  $2\sigma$ . For each map, the corresponding contribution to the total flux density uncertainty was taken to be the average value of all pixels encompassed by the GRG emission (i.e. cyan lines in Figs 2, 3, and 4).

The frequency attributed to each flux measurement is taken as that of the central spectral channel covered by the data. The exception to this is the *L*-band DR1 data, where the average effective frequency of the map has been accurately determined to be 1.284 GHz (see Hale

et al. 2024 for details). The effective frequencies at the positions of GRG1 ( $1.289 \pm 0.002$  GHz) and GRG2 ( $1.315 \pm 0.001$  GHz) are very similar to the average, and so we choose to use the average value of 1.284 GHz as the frequency of the *L*-band data throughout this work. This is for consistency with the measurements in the UHF subbands and in the COSMOS<sub>8</sub> *L* band (for GRG3), where more detailed effective frequency maps are not available. We have verified that using, for example, a frequency of 1.31 GHz for GRG2 does not change our results.

From Table 3, it can be seen that GRG3 has a significantly lower radio power than GRG1 and GRG2 at all frequencies.

### 3.2 Spectral indices and ages

We use Broadband Radio Astronomy Tools (BRATS) to estimate the spectral indices and spectral ages of the three GRGs on a pixel-by-pixel basis (Harwood et al. 2013; Harwood et al. 2015). BRATS takes flux-density maps at different frequencies and calculates the spectral index of each pixel using a least-squares regression in log space. BRATS can then convert spectral indices to spectral ages given various input parameters, such as the magnetic field strength ( $B$ ).

#### 3.2.1 Spectral index maps

We produce spectral index maps with BRATS using maps at the three frequencies 632, 755, and 1284 MHz. The resultant maps are shown in Fig. 5. GRG2 displays a spectral index map typical of an FR II, with a flat core ( $\alpha \sim 0.3$ ) and gradual steepening along the jets towards the outer ends of the lobes ( $\alpha > 2$ ). GRG1 displays a steeper core ( $\alpha \sim 0.6$ ) than what we expect, although it is still shallow relative to its lobes ( $\alpha < 1.6$ ). This indicates a possible restarted jet, which would be direct evidence of the duty cycle. GRG3, however, is relatively uniform in comparison. The majority of pixels have values in the range of  $0.4 < \alpha < 0.7$ . We do not see any resolved core, and the inner jets have an average of  $\alpha \sim 0.6$ .

#### 3.2.2 Magnetic fields

To calculate spectral ages, BRATS requires information on the magnetic field strength  $B$  in the GRG lobes. We estimate  $B$  using PYSYNCH<sup>4</sup> (Hardcastle, Birkinshaw & Worrall 1998), which models the synchrotron radiation and inverse Compton emission of radio galaxies assuming equipartition; that is, that the total energy densities

<sup>3</sup><https://github.com/ratt-ru/breizorro>

<sup>4</sup><https://github.com/mhardcastle/pysynch>



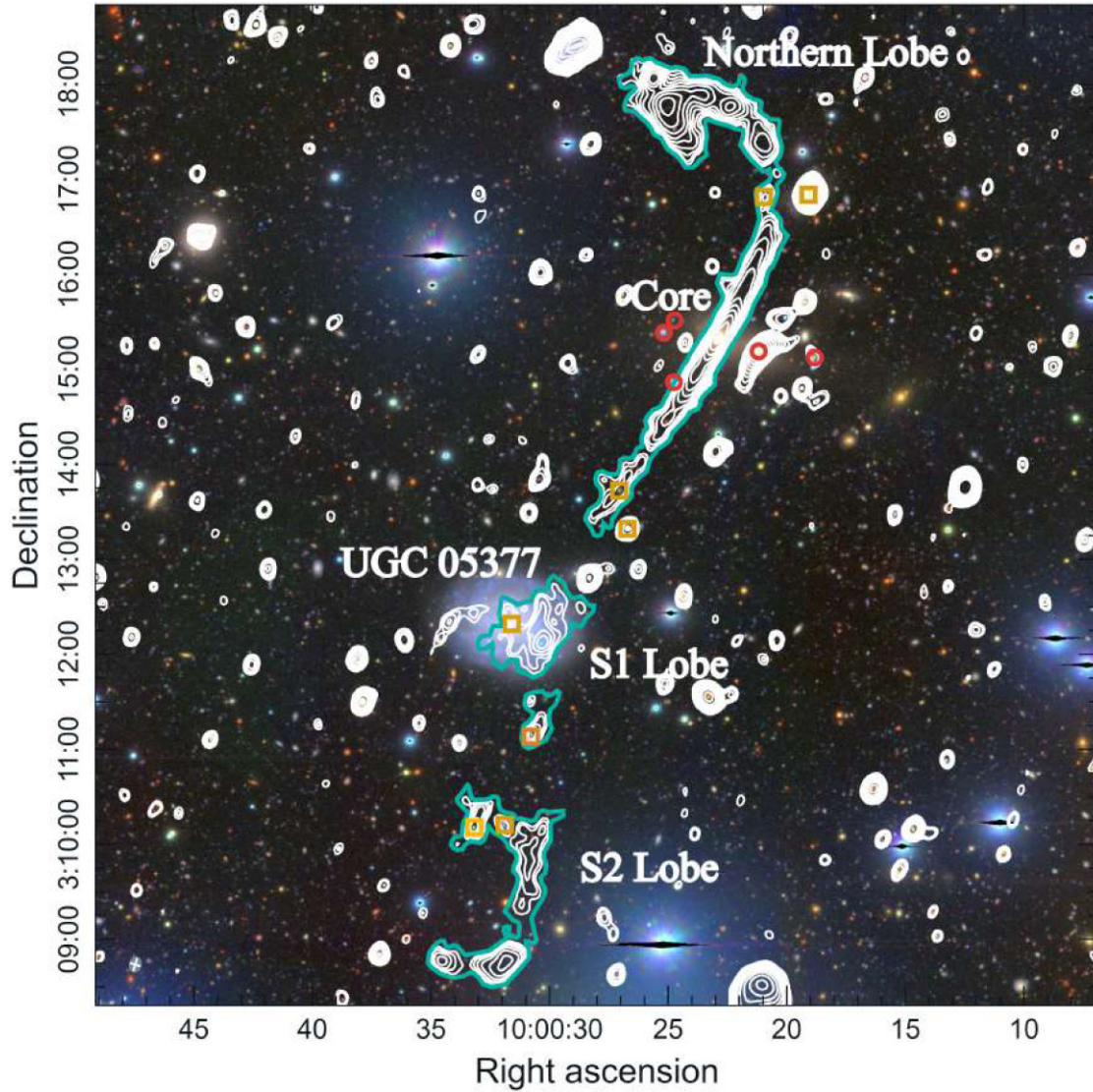


**Figure 1.** The optical HSC DR2 Wide combined  $g$ -,  $r$ -,  $i$ -band image of MGTC J100022.85+031520.4 (GRG3). Overlaid in white are radio contours from the COSMOS<sub>8</sub> map, which start at  $3\sigma = 2.91 \times 10^{-5}$  Jy beam<sup>-1</sup> and increase in steps of  $2''\sigma$  for  $n = 1, 2, 3, \dots, 15$ . The extent of GRG3, shown in cyan, is defined by the  $3\sigma$  contour, and important features are labelled. The S1 and S2 lobes represent the upper and lower portions of the southern lobe respectively. The five nearest spectroscopically confirmed cluster members are shown as red circles, and orange squares represent unrelated sources along the line of sight of the GRG, which have been accounted for in flux calculations.

**Table 2.** Basic properties of the COSMOS giant radio galaxies studied in this work. Columns: (1) object name; (2) right ascension (J2000); (3) declination (J2000); (4) spectroscopic redshift; (5) projected angular size, (6) projected linear size.

(1) Name	(2) RA (J2000)	(3) Dec. (J2000)	(4) $z_{\text{spec}}$	(5) $d$ (arcmin)	(6) $D$ (Mpc)
MGTC J095959.63+024608.6 (GRG1)	09 <sup>h</sup> 59 <sup>m</sup> 59.63 <sup>s</sup>	+ 02°46′08.6″	0.1656	13.8	2.42
MGTC J100016.84+015133.0 (GRG2)	10 <sup>h</sup> 00 <sup>m</sup> 16.84 <sup>s</sup>	+ 01°51′33.0″	0.3363	6.8	2.04
MGTC J100022.85+031520.4 (GRG3)	10 <sup>h</sup> 00 <sup>m</sup> 22.85 <sup>s</sup>	+ 03°15′20.4″	0.1034	12.0	1.29

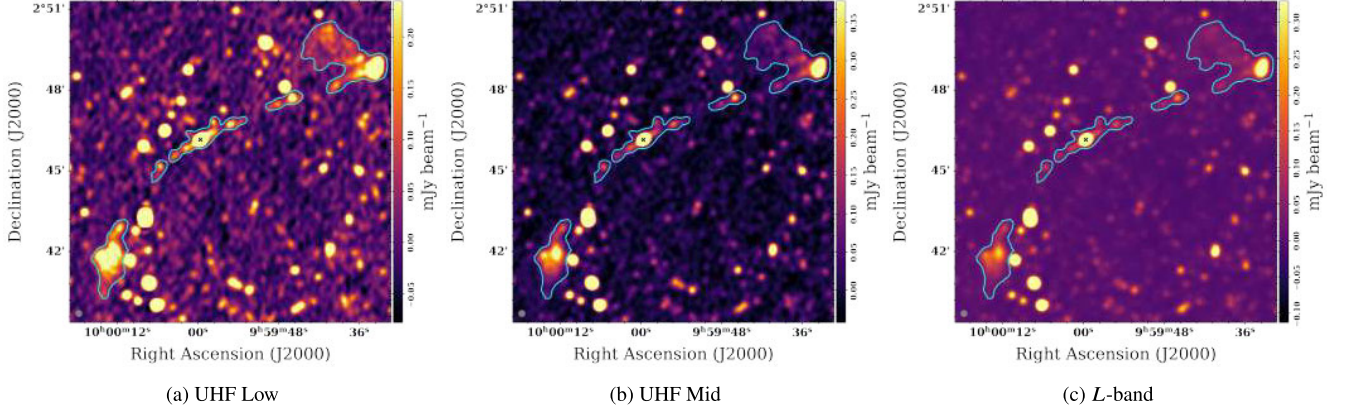


**Figure 2.** MeerKAT maps of GRG1 at 632, 755, and 1284 MHz (a, b, c respectively), each smoothed to a common resolution of  $14.02 \text{ arcsec} \times 14.02 \text{ arcsec}$ . The extent of the GRG, defined by the  $3\sigma$  contour at  $20.37 \mu\text{Jy beam}^{-1}$  in the *L* band, is shown in cyan. The beam is shown in grey in the bottom left corner of each image, and the location of the optical host AGN is shown as a black cross.

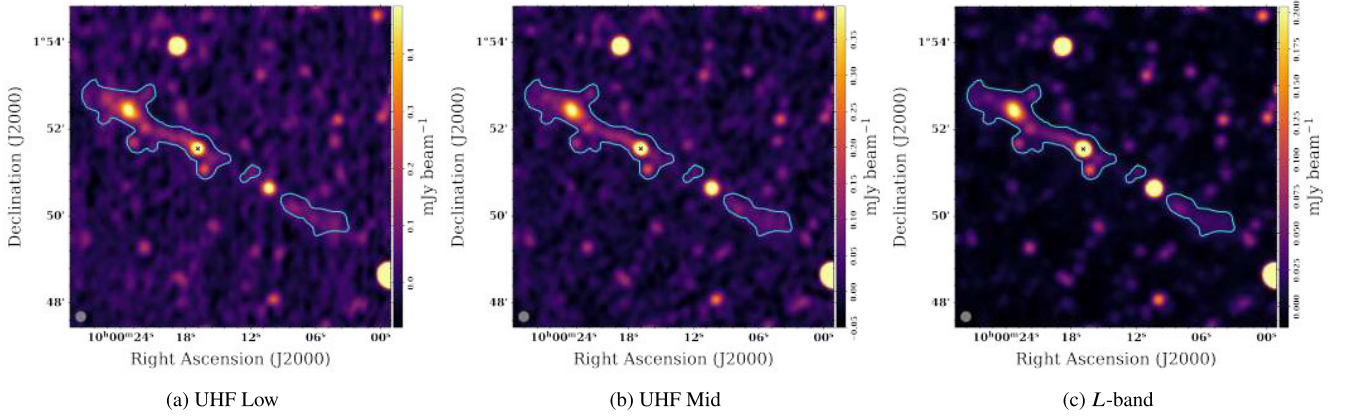


**Figure 3.** As Fig. 2, but for GRG2. The extent, marked in cyan, is taken at  $13.29 \mu\text{Jy beam}^{-1}$  in the *L* band.

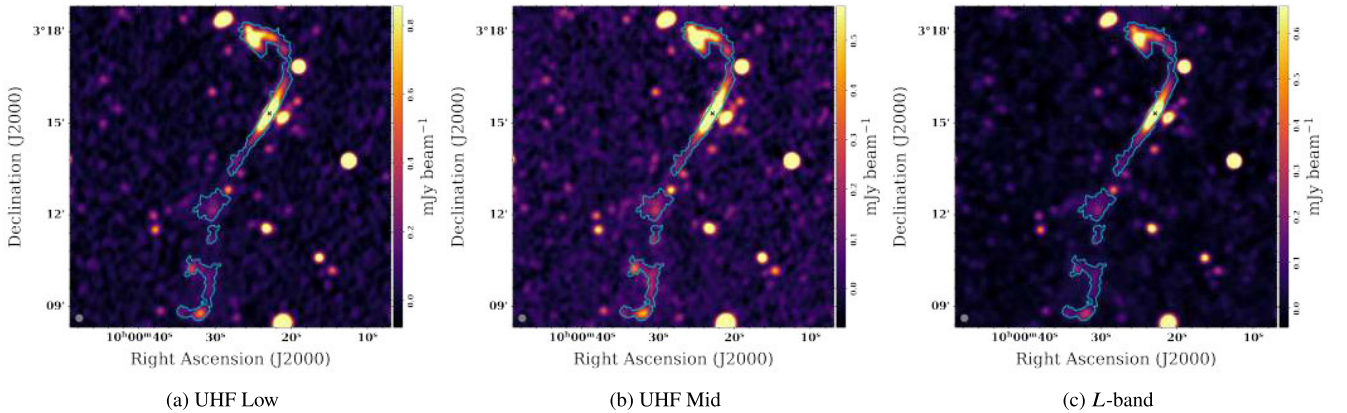


**Figure 4.** As Fig. 2, but for GRG3. The extent is defined at  $29.1 \mu\text{Jy beam}^{-1}$  in the *L* band and is shown in cyan.

of cosmic-ray electrons are equal to that of the magnetic field (Beck & Krause 2005). This assumption is made on the basis that cosmic-ray particles and magnetic fields are strongly coupled and exchange energy until equilibrium is reached. PYSYNCH approximates the radio lobe morphologies as ellipses and the radio continuum spectrum as a power law. For each GRG lobe, we find the total flux density within an ellipse drawn from the core to the end of the lobe. We then take the average of the semimajor axes, semiminor axes, and flux densities

of the two lobes for each GRG, and provide this to PYSYNCH. These input parameters are presented in Table 4.

The equipartition fields  $B_{\text{eq}}$  are 1.00, 0.95, and  $1.50 \mu\text{G}$  for GRGs 1, 2, and 3 respectively, giving an average equipartition magnetic field of  $B_{\text{eq}} = 1.15 \pm 0.02 \mu\text{G}$ . This is just in the range of  $B_{\text{eq}} \sim 1\text{--}16 \mu\text{G}$  of GRGs reported by Dabhade et al. (2023) in their review of GRG properties. However, recent observations have shown that the true magnetic field lies closer to 40 per cent of the equipartition value



**Table 3.** Integrated flux density and radio power of the GRGs in each band as well as the integrated spectral index values. Columns: (1) object name; (2, 3, 4) integrated flux density at 632, 755, and 1.28 GHz, respectively; (5) integrated spectral index calculated from the integrated flux density at 632 and 1284 MHz; (6, 7, 8) power at an effective frequency of 632, 755, and 1.28 GHz, respectively, determined using the spectral index in column 5.

(1) Name	(2) $S_{\text{int},632\text{MHz}}$ (mJy)	(3) $S_{\text{int},755\text{MHz}}$ (mJy)	(4) $S_{\text{int},1284\text{MHz}}$ (mJy)	(5) $\alpha_{632\text{MHz}}^{1284\text{MHz}}$	(6) $P_{632\text{MHz}}$ ( $10^{24} \text{ W Hz}^{-1}$ )	(7) $P_{755\text{MHz}}$ ( $10^{24} \text{ W Hz}^{-1}$ )	(8) $P_{1284\text{MHz}}$ ( $10^{24} \text{ W Hz}^{-1}$ )
GRG1	$33.20 \pm 2.00$	$29.10 \pm 1.70$	$19.10 \pm 1.10$	$0.78 \pm 0.12$	$2.590 \pm 0.270$	$2.230 \pm 0.230$	$1.490 \pm 0.160$
GRG2	$7.47 \pm 0.53$	$5.98 \pm 0.45$	$3.88 \pm 0.25$	$0.92 \pm 0.13$	$3.000 \pm 0.350$	$2.090 \pm 0.240$	$1.380 \pm 0.160$
GRG3	$32.30 \pm 2.00$	$28.70 \pm 1.80$	$21.20 \pm 1.30$	$0.59 \pm 0.12$	$0.890 \pm 0.092$	$0.802 \pm 0.082$	$0.597 \pm 0.061$

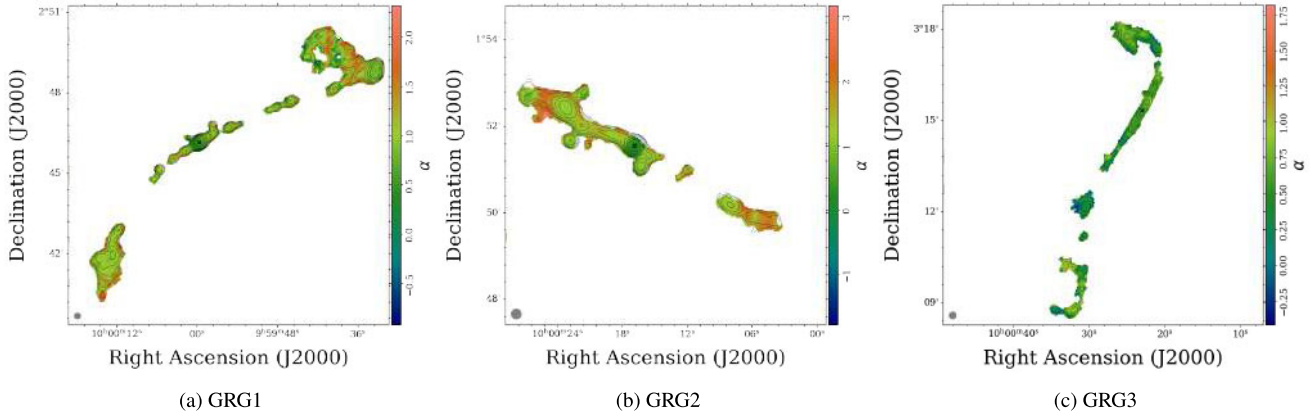


**Figure 5.** Spectral index maps of the giant radio galaxies as created in BRATS. Panel (a) has estimated spectral indices within the range  $-0.58 \leq \alpha \leq 2.14$ . Panel (b) contains values in the range  $-0.06 \leq \alpha \leq 3.18$ . Panel (c) has a spectral index range of  $-0.42 \leq \alpha \leq 1.33$ . The colour bars show the full range of indices in each case. Shown in black are the overlaid contours of the corresponding  $L$  map, starting at  $3\sigma$  and increasing with intervals of  $2^n\sigma$ , where  $n = 0, 1, \dots, 15$ . The beam is indicated in grey in the bottom left corner.

**Table 4.** Input parameters for the PYSYNCH code to calculate the equipartition energy and the final magnetic fields. Columns: (1) name of the source; (2) semimajor axis of the ellipse used to estimate the lobe size; (3) semiminor axis of the ellipse; (4) flux density as dictated by the ellipse; (5) final magnetic field, which is taken to be  $0.4B_{\text{eq}}$ , where  $B_{\text{eq}}$  is the equipartition field given by PYSYNCH.

(1) Name	(2) $a$ (arcsec)	(3) $b$ (arcsec)	(4) $S_{\nu}$ (mJy)	(5) $B$ ( $\times 10^{-1} \mu\text{G}$ )
GRG1	90	64	9.79	4.18
GRG2	63	45	2.56	3.80
GRG3	60	45	8.65	5.87

(Croston et al. 2005; Ineson et al. 2017; Mahatma et al. 2019). We therefore assume that the magnetic fields of the GRGs are  $0.4B_{\text{eq}}$ , where  $B_{\text{eq}}$  is the equipartition magnetic field strength. The final magnetic fields  $B = 0.4B_{\text{eq}}$  are also shown in Table 4.

### 3.2.3 Spectral ages

The spectral age maps for the three GRGs are determined with the maps at 632, 755, and 1284 MHz using two of the single-injection models within BRATS: the standard Jaffe–Perola model (JP; Jaffe & Perola 1973) and the JP–Tribble model (Tribble 1993). Both models assume that the initial electron energy distribution is described as a power law  $N(E) = N_0 E^{-2\alpha_{\text{inj}}-1}$ , where  $2\alpha_{\text{inj}} + 1$  is the power-law index of the initial injected energy distribution, and assume the losses for the distribution as synchrotron self-absorption and inverse

Compton losses. Both models need the redshift of the galaxy, the magnetic field, and the injection index ( $\alpha_{\text{inj}}$ ). The models differ in that the standard JP model applies a constant magnetic field, while the Tribble method varies the magnetic field in space by applying a Gaussian random field to the source, so that the electrons diffuse over spatial regions of various magnetic field strengths. BRATS accounts for magnetic field losses due to the cosmic microwave background in both models. The Tribble method has been shown to be more physically plausible than the JP method (Harwood et al. 2013; Harwood et al. 2015); however, it is much more computationally expensive. While an analysis of both was feasible for the small sample of three GRGs, ensuring that the standard JP method is in agreement with the Tribble estimates would be beneficial for future studies. For a more in-depth explanation of the two methods, see Harwood et al. (2015) and Harwood et al. (2013).

For the spectral age fitting, a circular background region of 30 arcsec in diameter was used to calculate the flux-density image rms noise. The spectral age of a given pixel is set to be calculated only if there is a flux density above  $1\sigma$  in every input frequency, owing to the UHF subbands having lower signal-to-noise ratios than the  $L$ -band image. The flux calibration uncertainty is set to be 10 per cent, which is the standard for BRATS calculations. The age resolution is set as 10 Myr with a 5-level iteration, with a maximum age of 150 Myr and a minimum of 0 Myr as reasonable bounds.

Because the injection index of GRGs has yet to be observationally constrained, we adopt a constant injection index of  $\alpha_{\text{inj}} = 0.5$ . This is chosen in accordance with Bell (1978) and Carilli et al. (1991) as the lowest value that can be theoretically observed and is a common value used in the literature. Because recent studies (Harwood et al.

2013) have shown that injection indices can be as high as  $\sim 0.8$ , a preliminary estimate of the injection index was carried out with BRATS. The three GRGs in this study were found to have values in the range  $0.5 < \alpha_{\text{inj}} < 0.65$ , ensuring that  $\alpha_{\text{inj}} = 0.5$  is an appropriate choice. We note that if the chosen injection index is artificially low, it will artificially increase the absolute values of the calculated spectral ages; however, it will not affect the *relative* distribution of ages throughout a source.

The resultant spectral age maps as calculated by both the JP standard and Tribble models are shown in Figs 6, 7, and 8. The average ages of each component are given in Table 5. Uncertainties for the spectral ages are taken from uncertainty maps produced by BRATS for each model. BRATS also calculates spectral age uncertainties on a pixel-by-pixel basis. In Figs 6 and 7, we overlay contours connecting pixels with spectral age uncertainties of 20, 30, and 40 per cent for GRG1 and GRG2. The contours in Fig. 8 represent the 40, 60, and 80 per cent uncertainties for GRG3. Possible reasons for these larger spectral age uncertainties are discussed in Section 4.1. Both models give a similar distribution of spectral ages to each other and to their respective spectral index maps, which is expected and which suggests that in future studies the JP method may be adequate for spectral age analyses. The Tribble method gives slightly higher age estimates (with the difference in values being more pronounced at higher ages). However, it can be seen from Table 5 that the values agree with one another within their uncertainty budgets. For all three GRGs, the youngest ages are seen in the centre and in the hotspots of the GRG, with older electrons in the lobes surrounding the hotspots as well as in the jets, as expected.

## 4 DISCUSSION

### 4.1 Distribution of spatially resolved spectral ages

According to the JP model, GRG1 has a maximum age of  $60 \pm 11$  Myr. This is the maximum pixel value, found in the lobes, in the spectral age map shown in Fig. 6. The core displays the youngest electrons (relating to GRG emission) with a value of  $2.0 \pm 15$  Myr, that is, consistent with a zero age. The northern hotspot shows a mean age of  $25.7 \pm 7.6$  Myr, and the rest of the lobe is slightly older, with a value of  $40.0 \pm 8.1$  Myr, giving the average value shown in the table of  $\sim 35$  Myr, signalling an injection of energy at the hotspot owing to a collision with the IGM. The values here are calculated only including regions where the spectral age uncertainties are less than 30 per cent, as shown in Fig. 6. This is to ensure that the ages are not underestimated, as BRATS tends to assign low ages in regions where the spectral ageing model is poorly constrained. The southern lobe displays similar ages to the northern lobe, with an average JP age of  $33 \pm 7.55$  Myr, consistent with the assumption that the two lobes were created at the same time and are in a similar environment.

Because the core of GRG2 displays a flat spectral index, it is likely dominated by synchrotron self-absorption and therefore cannot be well constrained by the power-law models employed by BRATS. The spectral ages calculated in this region by BRATS are therefore unreliable, and thus have been masked out of the spectral age map in Fig. 7. The northern lobe and hotspot together have an average JP age of  $22.7 \pm 4.2$  Myr and a Tribble age of  $24.7 \pm 4.4$  Myr, which agree with the southern lobe ages of  $25.7 \pm 6.3$  Myr using the JP model and  $28.4 \pm 6.8$  Myr using the Tribble model. The maximum Tribble age is  $47.0 \pm 11$  Myr. The JP and Tribble models are both better constrained for GRG2 than for the other two GRGs, based on the uncertainties reported by BRATS. GRG2 also displays the most

typical FR II morphology and expected spectral index distribution, implying that such properties are best modelled by BRATS.

GRG3, on the other hand, presents a much more interesting case. The uncertainties for GRG3 are twice as large as those for the other two GRGs, which is likely owing to GRG3 being located towards the edge of the UHF field of view. Using the low-sensitivity COSMOS<sub>8</sub>L-band map rather than the deeper mosaic of DR1 most likely also contributes to the uncertainties shown. Because of this, we extend our limits used for our calculations to include all pixels for which the uncertainty is below 60 per cent of the computed age. We do see slightly younger ages in the core ( $13 \pm 18$  Myr with the JP model) compared with the centre of the lobes ( $27 \pm 22$  and  $47 \pm 21$  Myr for the northern and southern lobes, respectively). However, the youngest ages in GRG3 are seen in the diffuse outer plasma. This is contrary to expectations, because these regions are far from the expected particle acceleration sites in the inner jets. The minimum ages in these outer plasma regions are  $\sim 0$  Myr; however, we caution that the uncertainties are even larger in this region ( $\sim 50$  Myr). We also see recently accelerated plasma surrounding UGC 05377 and conclude that these values are at least partially contaminated by the star-forming galaxy. The maximum JP age for GRG3 is  $64 \pm 31$  Myr, and the maximum Tribble age is  $67 \pm 36$  Myr.

There is still, however, the matter of the aged core and the only slight steepening in the lobes. While the distribution of spectral indices and ages of GRG3 do not resemble those of a typical GRG, there are similarities in the distribution of ages within WAT galaxies (Giacintucci et al. 2008; Pandge et al. 2022). Potentially, the dense environment found within both WAT galaxies and GRG3 is contributing to the distribution seen (Enßlin & Gopal-Krishna 2001; Kempner & Sarazin 2001) and might even contribute to the large uncertainties. The slightly older core could mean that the central engine has recently switched off and the galaxy is entering a period of quiescence. However, more likely, it suggests that the injection index is instead higher than what we have assumed and so all ages have been increased. More sensitive observations at a range of frequencies are needed to constrain this degeneracy. This, however, does not affect the distribution of ages shown.

### 4.2 Comparison with dynamical estimates

We compare the power and size of the COSMOS GRGs with those of others in the literature. Specifically, we compare with the GRG compilation catalogue of Dabhade et al. (2023) and the LOTSS DR2 optically matched source catalogue of Hardcastle et al. (2023). The latter contains accurate flux densities for many of the GRGs presented in Simonte et al. (2022), Oei et al. (2023), Simonte et al. (2024), and Mostert et al. (2024). The combined total is  $\sim 9000$  GRGs; see Fig. 9. The COSMOS GRGs are shown as stars and occupy the lower right-hand corner of the diagram, showing that they are still below the sensitivity limit of LOFAR, and are some of the largest and lowest-luminosity GRGs detected. We use the power–diameter (P-D) diagram to determine the dynamical age of the galaxies as an independent comparison to the spectral age. The dynamical age is estimated based on the size, power, and environment of a galaxy.

For the GRGs, we estimate the dynamical age using the ANALYTIC<sup>5</sup> model from Hardcastle (2018), shown in Fig. 9 as evolutionary tracks. The ANALYTIC model derives a number of properties of a radio galaxy, including its power and diameter, as a function of time. It assumes a density profile for the environment, as well as the power of the

<sup>5</sup><https://github.com/mhardcastle/analytic>



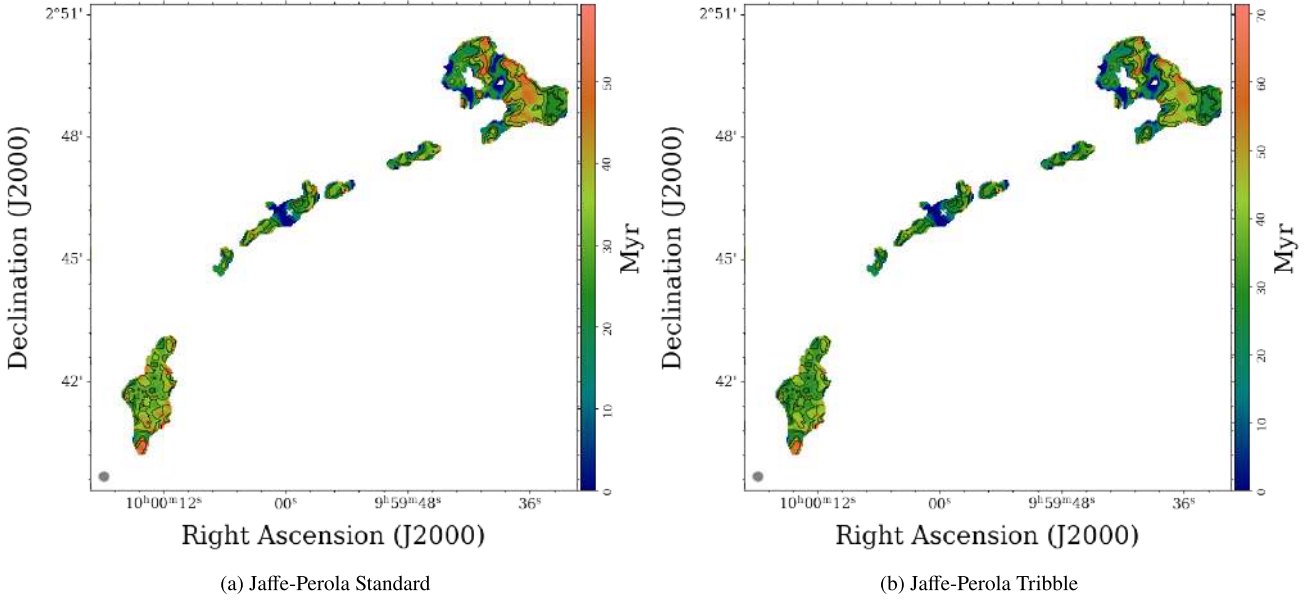


**Figure 6.** Spectral ages for GRG1 as determined by BRATS using different fitting models with  $L$ -band contours overlaid (see Figs 2 and 5a for details). The models were run using an injection index of 0.5 and a magnetic field of  $0.418 \mu\text{G}$ . The maximum JP age is  $60 \pm 11$  Myr, and the maximum Tribble age is  $68 \pm 13$  Myr. Percentage uncertainty contours are shown in black at 20 per cent, 30 per cent, and 40 per cent.

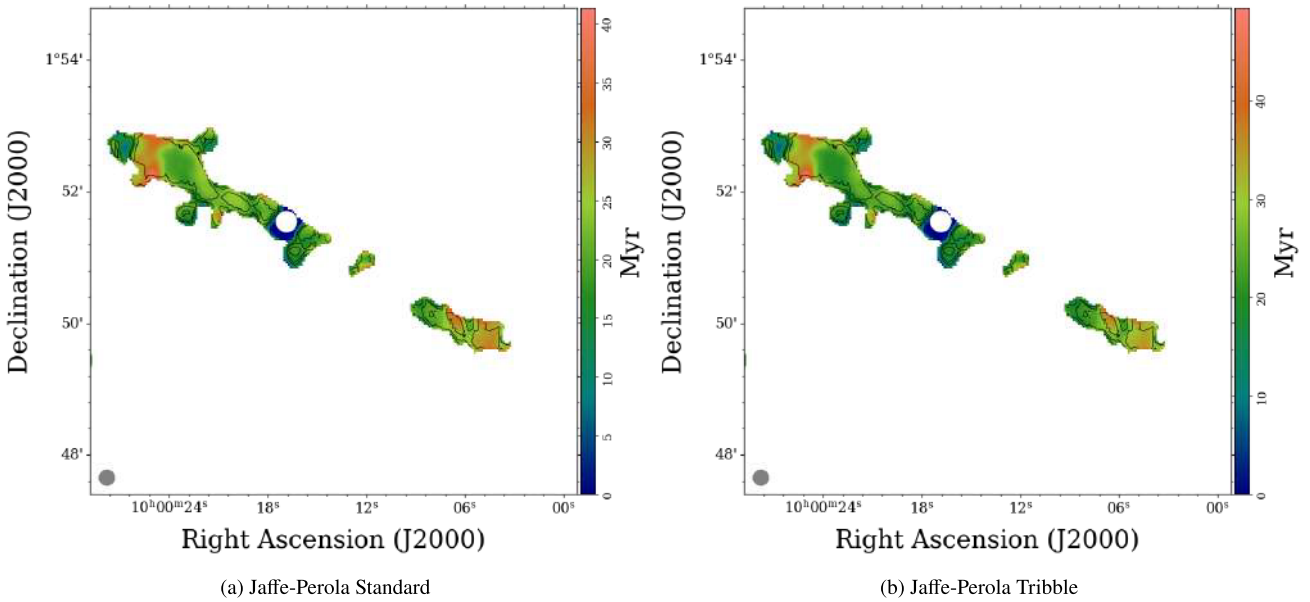


**Figure 7.** As Fig. 6, but for GRG2. The magnetic field is  $0.380 \mu\text{G}$ , and the resulting maximum ages are  $39.2 \pm 7.5$  and  $47.0 \pm 11.0$  Myr according to the JP and JP Tribble models, respectively. Percentage uncertainty contours are shown in black at 20 per cent, 30 per cent, and 40 per cent.

jets. For the GRGs, the universal pressure profile from Arnaud et al. (2010) is used, with the functional form of

$$P(r) = P_{500} \left[ \frac{M_{500}}{3 \times 10^{14} h_{70}^{-1} M_{\odot}} \right]^{\alpha_p + \alpha'_p(x)} p(x), \quad (1)$$

where  $x = r/R_{500}$  and  $p(x)$  is a generalized Navarro–Frenk–White profile. This profile is chosen as it has been shown to represent the pressure profile of poor-cluster/big-group galaxies. It also has the added advantage of only having one free parameter:  $M_{500}$ , the total mass in a radius that corresponds to 500 times the critical density of the Universe.

The density of the environment  $M_{500}$  for GRG1 and GRG2 is estimated using the number density of galaxies within a  $1.5\text{-Mpc } h^{-1}$  radius. GRG1 and GRG2 reside in small groups containing eight and five members, respectively, according to the zCOSMOS 20k group catalogue (Knobel et al. 2012). Neither of these groups has enough spectroscopic redshift members ( $N > 5$ ) for accurate velocity dispersion rates, and so a lower limit of  $M_{500} = 10^{13} M_{\odot}$  is assumed (Reiprich et al. 2013; Ineson et al. 2015). The  $M_{500}$  value for GRG3 is taken directly from Wen et al. (2012) to be  $M_{500} = 9.3 \times 10^{13} M_{\odot}$ . The dynamical estimates are shown in Fig. 9 as evolutionary tracks. Using these mass estimates, the best-fitting tracks are determined

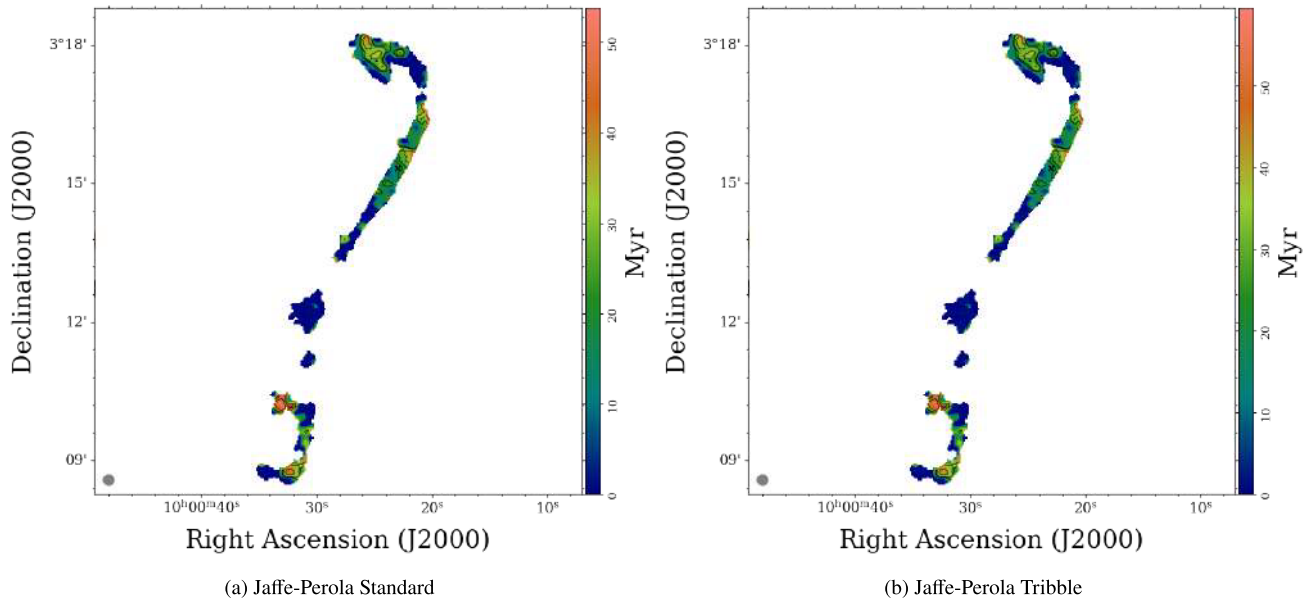


**Figure 8.** As Fig. 6, but for GRG3. The magnetic field is  $0.587 \mu\text{G}$ , and the resulting maximum ages are  $64 \pm 31$  and  $67 \pm 36$  Myr according to the JP and JP Tribble models, respectively. Percentage uncertainty contours are shown in black at 40 per cent, 60 per cent, and 80 per cent.

**Table 5.** Measured average spectral ages within the core and lobes of the GRGs. Columns: (1) source; (2) model of spectral ageing; (3, 4, 5) average spectral age in the core or inner jets in the case of GRG3, and the northern and southern lobes, respectively.

(1) Source	(2) Model	(3) Core/inner jets (Myr)	(4) Northern lobe (Myr)	(5) Southern lobe (Myr)
GRG1	JP	$2^{+15.0}_{-2.8}$	$35.2^{+7.2}_{-9.3}$	$32.9^{+6.8}_{-8.3}$
	Tribble	$3^{+14.0}_{-2.1}$	$37.6^{+7.5}_{-9.5}$	$34.5^{+7.9}_{-9.0}$
GRG2	JP	-	$22.7^{+3.5}_{-4.2}$	$25.7^{+5.0}_{-6.3}$
	Tribble	-	$24.7^{+3.4}_{-4.4}$	$28.4^{+5.3}_{-6.8}$
GRG3	JP	$13.0^{+17.0}_{-18.0}$	$27.0^{+15.0}_{-23.0}$	$42^{+17.0}_{-29.0}$
	Tribble	$14^{+19.0}_{-13.0}$	$29^{+15.0}_{-23.0}$	$44^{+20.0}_{-30.0}$

empirically. These tracks imply that GRG1 and GRG2 are consistent with the evolution of a galaxy with a jet power of  $P_j \sim 10^{38}$  W after  $\sim 800$  and  $\sim 700$  Myr, respectively. The suggested ages for GRG3 are consistent with the evolution of a  $P_j \sim 10^{36}$  W jet after  $\sim 950$  Myr.

The evolution of the GRGs in ANALYTIC is derived assuming that the jets at no point switch off. For GRG3, if we instead assume that the jets have turned off recently, as potentially implied by the spectral ages in the core, the estimated jet power would increase, and the dynamical age of GRG3 would decrease. This, however, adds an extra level of degeneracy to the model, because unless the true age before turn-off is known, there is no constraint on the jet power. Thus, GRG3 would be equally well represented by a young source with a jet power of  $P_j \sim 10^{39}$  W with a dynamical age of  $\sim 300$  Myr. Hence, we simply keep the calculated dynamical age of GRG3 as an upper limit.

Comparing the maximum Tribble ages with their dynamical counterparts, the dynamical ages are many times larger than their

spectral counterparts, although there are some known discrepancies between spectral and dynamical age that warrant consideration.

The spectral ages of galaxies are mainly dependent on two parameters: the break frequency and the magnetic field. The magnetic field strength of galaxies is not trivial to determine, and the distribution and evolution of the magnetic field are much more complicated than what even the Tribble model assumes. The magnetic field will decrease over time and will most likely be higher at the core and the hotspots where the electrons originate before they permeate into the surrounding environment. This may contribute to the discrepancies between spectral and dynamical ages.

Another source of uncertainty is that the spectral age models do not consider other loss mechanisms in the lobes, such as adiabatic cooling, nor the effects of electron mixing. Adiabatic losses within a galaxy would result in an overestimation of the spectral ages within the plasma (Blundell et al. 1999). Electron mixing describes the phenomenon that even the faintest radio emission traces electron populations of different energies (Turner et al. 2018; Mahatma et al. 2019). Electron mixing biases age towards younger estimates and is considered to be the cause of spectral ages at subequipartition magnetic fields still being at most half of their dynamical counterparts (Mahatma et al. 2019).

Furthermore, the dynamical ages are limited without true knowledge of the jet power and the proper length, although they are fairly robust against changes to these parameters. The dynamical age is, however, very sensitive to changes in the density of the environment, with an order of magnitude increase in density increasing the dynamical age by a factor of  $\sim 2$ .

Taking these limitations into account does not entirely reconcile the spectral ages with the dynamical ages, even with an estimate of the environment. Thus, we conclude, similarly to Mahatma et al. (2020) and Pinjarkar et al. (2023), that there are extra processes that either or both spectral and dynamical models do not account for. The contamination from electron mixing has not been very well constrained in GRGs and could be playing an increased role here.

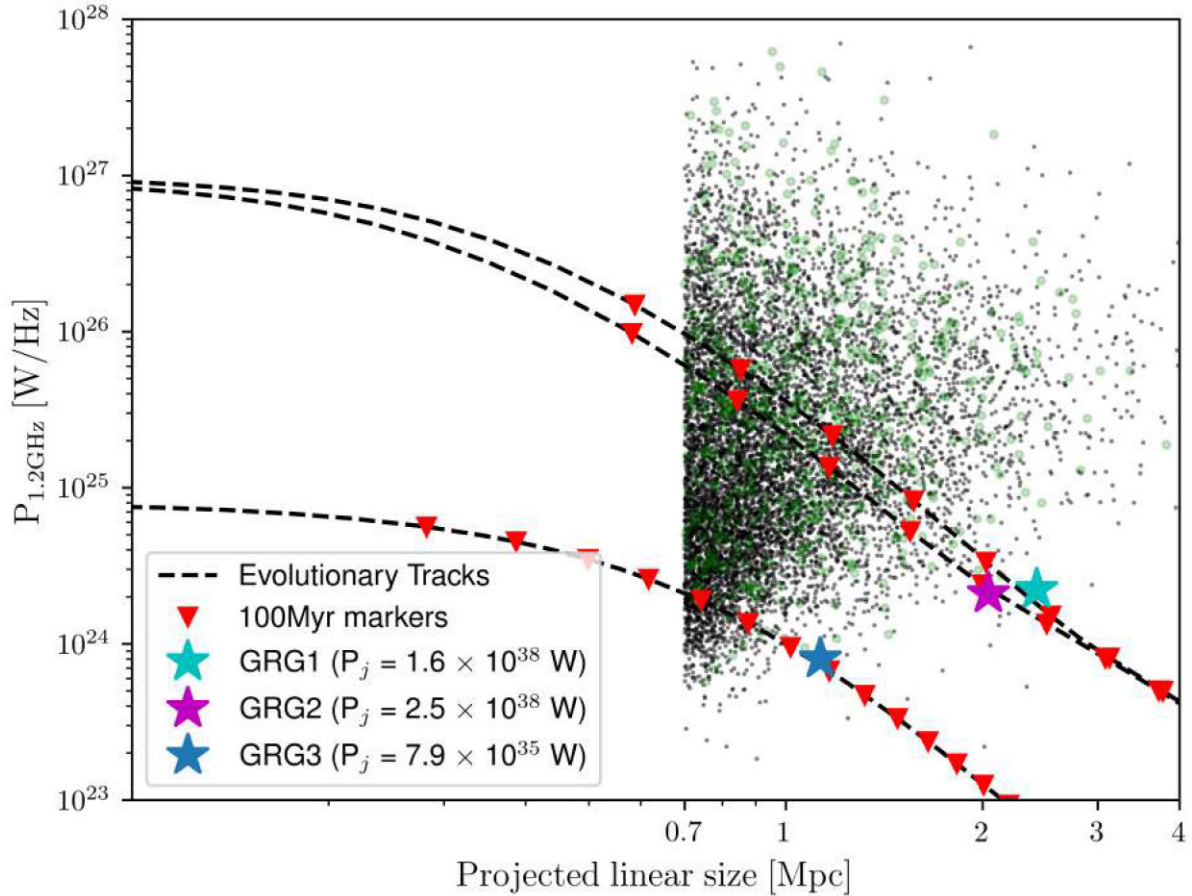


**Figure 9.** The 1.28-GHz power–diameter (P-D) diagram of the COSMOS GRGs compared with the literature. Objects in the compilation catalogue of Dabhade et al. (2020) are shown as green points, and sources from Hardcastle et al. (2023) are shown in black. The MIGHTEE GRGs are shown as different-coloured stars and are in the lower right-hand corner of the diagram. The black lines are evolutionary tracks generated with Hardcastle (2018), which correspond to an idealized evolution of each GRG. The red triangles mark each hundred Myr, with the leftmost triangle on each track corresponding to 300 Myr. The jet powers for each track are given next to the corresponding GRG label.

## 5 SUMMARY AND CONCLUSIONS

We have presented spatially resolved spectral index and age maps of three GRGs within the COSMOS field using MIGHTEE *L*-band data and new MeerKAT UHF-band observations. MGTC J100022.85+031520.4, dubbed GRG3, is presented here for the first time. We summarize our main results here.

(i) MGTC J100022.85+031520.4 (GRG3) is a GRG located in the northernmost part of the COSMOS primary beam in the UHF band of MeerKAT. It is hosted by the elliptical galaxy SDSS J100022.85+031520 with a redshift of  $z = 0.1034 \pm 0.00002$ . It has a projected linear size of 1.29 Mpc and a total power at 1284 MHz of  $5.97 \pm 0.02 \times 10^{23} \text{ W Hz}^{-1}$ . Its features are similar to those of a WAT galaxy.

(ii) The spectral analysis was performed using two different models: the JP standard model and the Tribble model. The two models agreed with each other within their uncertainties, with the Tribble model consistently producing older estimates of the electron ages within the sources.

(iii) GRG1 was found to have the oldest electrons, with a maximum Tribble age of  $68 \pm 13$  Myr and a mean Tribble lobe age of 34 Myr. GRG3 has a maximum (Tribble) lobe age of  $\sim 67$  Myr, and GRG2 has the youngest maximum Tribble age of  $\sim 47$  Myr in the lobes.

(iv) Based on the spectral age distribution, GRGs 1 and 2 are likely to still be active. The steep spectral index in the core of GRG1 indicates a restarted jet.

(v) The distribution of ages within the GRGs showcases the history of their evolution. GRGs 1 and 2 have been able to grow in relatively isolated environments and thus have the expected distribution of ages, with the youngest age in the core and the oldest in the lobes. GRG3, however, shows more complexity, possibly owing to its being in a denser cluster environment and having more interactions with its surroundings.

(vi) Dynamically, GRG3 was found to be consistent with a galaxy of  $P_j \sim 10^{36} \text{ W}$  jet power that is  $\sim 950$  Myr old, while GRGs 1 and 2 are consistent with 800- and 700-Myr-old galaxies with jet powers of  $P_j \sim 10^{38} \text{ W}$ . These ages are many times larger than their spectral counterparts, indicating that there are processes unaccounted for in either the spectral or dynamical age estimates.

(vii) This work demonstrates the various limitations of the spectral age calculations and the discrepancies between the spectral ages and dynamical ages. However, it also shows that the relative ages determined through spectral ageing are valuable in determining the dynamics and evolution of GRGs through the distribution of electron ages throughout the GRG.



## ACKNOWLEDGEMENTS

We thank the anonymous referee for useful suggestions, which improved this paper. KC's research is supported by the South African Radio Astronomy Observatory (SARAO). JD, KC, MJ, and IH acknowledge support from an Africa–Oxford Catalyst Collaboration Grant (AfOx-290), which made this research possible. JD also acknowledges support from a UCT Research Development Grant. MJJ, IHW, and CLH acknowledge generous support from the Hintze Family Charitable Foundation through the Oxford Hintze Centre for Astrophysical Surveys. MJJ and IH also acknowledge support from a UKRI Frontiers Research Grant (EP/X026639/1), which was selected by the ERC, and the UK Science and Technology Facilities Council (ST/S000488/1). FXA acknowledges support from the National Natural Science Foundation of China (12303016) and the Natural Science Foundation of Jiangsu Province (BK20242115). ID acknowledges funding from the European Union – NextGenerationEU, RRF M4C2 1.1, PRIN 2022JZJBHM: 'AGN-sCAN: zooming-in on the AGN-galaxy connection since the cosmic noon' – CUP C53D23001120006. The MeerKAT telescope is operated by the South African Radio Astronomy Observatory, which is a facility of the National Research Foundation, an agency of the Department of Science and Innovation. We acknowledge the use of the ilifu cloud computing facility, [www.ilifu.ac.za](http://www.ilifu.ac.za), a partnership between the University of Cape Town, the University of the Western Cape, Stellenbosch University, Sol Plaatje University, and the Cape Peninsula University of Technology. The ilifu facility is supported by contributions from the Inter-University Institute for Data Intensive Astronomy (IDIA, a partnership between the University of Cape Town, the University of Pretoria, and the University of the Western Cape), the Computational Biology division at UCT, and the Data Intensive Research Initiative of South Africa (DIRISA). This work made use of the CARTA (Cube Analysis and Rendering Tool for Astronomy) software (DOI 10.5281/zenodo.3377984 – <https://cartavis.github.io>). Funding for SDSS-III has been provided by the Alfred P. Sloan Foundation, the Participating Institutions, the National Science Foundation, and the US Department of Energy Office of Science. The SDSS-III website is <http://www.sdss3.org>. SDSS-III and is managed by the Astrophysical Research Consortium for the Participating Institutions of the SDSS-III Collaboration, including the University of Arizona, the Brazilian Participation Group, Brookhaven National Laboratory, Carnegie Mellon University, University of Florida, the French Participation Group, the German Participation Group, Harvard University, the Instituto de Astrofísica de Canarias, the Michigan State/Notre Dame/JINA Participation Group, Johns Hopkins University, Lawrence Berkeley National Laboratory, Max Planck Institute for Astrophysics, Max Planck Institute for Extraterrestrial Physics, New Mexico State University, New York University, Ohio State University, Pennsylvania State University, University of Portsmouth, Princeton University, the Spanish Participation Group, University of Tokyo, University of Utah, Vanderbilt University, University of Virginia, University of Washington, and Yale University. This work is based on the research supported in part by the National Research Foundation of South Africa (Grant Number 151060). The Hyper Suprime-Cam (HSC) collaboration includes the astronomical communities of Japan and Taiwan, and Princeton University. The HSC instrumentation and software were developed by the National Astronomical Observatory of Japan (NAOJ), the Kavli Institute for the Physics and Mathematics of the Universe (Kavli IPMU), the University of Tokyo, the High Energy Accelerator Research Organization (KEK), the Academia Sinica Institute for Astronomy and Astrophysics in Taiwan (ASIAA), and Princeton

University. Funding was contributed by the FIRST program from the Japanese Cabinet Office, the Ministry of Education, Culture, Sports, Science and Technology (MEXT), the Japan Society for the Promotion of Science (JSPS), the Japan Science and Technology Agency (JST), the Toray Science Foundation, NAOJ, Kavli IPMU, KEK, ASIAA, and Princeton University.

## DATA AVAILABILITY

The data underlying this article were accessed from the South African Radio Astronomy Observatory (SARAO; [www.sarao.ac.za](http://www.sarao.ac.za)). Upon publication, the radio images from MIGHTEE DR1 will be accessible through: <https://doi.org/10.48479/7msw-r692>. The MeerKAT UHF-COSMOS fits image cutouts generated in this research will be shared upon reasonable request: please contact the PI of the data (J. Delhaize; [drjdelhaize@gmail.com](mailto:drjdelhaize@gmail.com)). The raw MeerKAT visibilities for which any proprietary period has expired can be obtained from the SARAO archive at <https://archive.sarao.ac.za>.

## REFERENCES

- Adelman-McCarthy J. K. et al., 2008, *ApJS*, 175, 297  
 Aihara H. et al., 2018, *PASJ*, 70, S8  
 Albareti F. D. et al., 2017, *ApJS*, 233, 25  
 Arnaud M., Pratt G. W., Piffaretti R., Böhringer H., Croston J. H., Pointecouteau E., 2010, *A&A*, 517, A92  
 Beck R., Krause M., 2005, *Astron. Nachrichten*, 326, 414  
 Bell A. R., 1978, *MNRAS*, 182, 147  
 Blundell K. M., Rawlings S., 2000, *AJ*, 119, 1111  
 Blundell K. M., Rawlings S., Willott C. J., 1999, *AJ*, 117, 677  
 Bower R. G., Benson A. J., Malbon R., Helly J. C., Frenk C. S., Baugh C. M., Cole S., Lacey C. G., 2006, *MNRAS*, 370, 645  
 Burns J. O., 1990, *AJ*, 99, 14  
 Carilli C., Perley R., Dreher J., Leahy J., 1991, *ApJ*, 383, 554  
 Croston J. H., Hardcastle M. J., Harris D. E., Belsole E., Birkinshaw M., Worrall D. M., 2005, *ApJ*, 626, 733  
 Croton D. J. et al., 2006, *MNRAS*, 365, 11  
 Dabhade P. et al., 2020, *A&A*, 642, A153  
 Dabhade P., Saikia D. J., Mahato M., 2023, *JA&A*, 44, 13  
 Delhaize J. et al., 2021, *MNRAS*, 501, 3833  
 Enßlin T. A., Gopal-Krishna, 2001, *A&A*, 366, 26  
 Fabian A. C., 2012, *ARA&A*, 50, 455  
 Fanaroff B. L., Riley J. M., 1974, *MNRAS*, 167, 31P  
 Giacintucci S. et al., 2008, *ApJ*, 682, 186  
 Gopal-Krishna Wiita P., Saripalli L., 1989, *MNRAS*, 239, 173  
 Hale C. L. et al., 2024, *MNRAS*, <https://doi.org/10.1093/mnras/stae2528>  
 Hardcastle M. J. et al., 2019, *A&A*, 622, A12  
 Hardcastle M. J. et al., 2023, *A&A*, 678, A151  
 Hardcastle M. J., 2018, *MNRAS*, 475, 2768  
 Hardcastle M. J., Birkinshaw M., Worrall D. M., 1998, *MNRAS*, 294, 615  
 Harwood J. J., Hardcastle M. J., Croston J. H., 2015, *MNRAS*, 454, 3403  
 Harwood J. J., Hardcastle M. J., Croston J. H., Goodger J. L., 2013, *MNRAS*, 435, 3353  
 Heckman T. M., Best P. N., 2014, *ARA&A*, 52, 589  
 Heywood I. et al., 2022, *MNRAS*, 509, 2150  
 Heywood I., 2020, Astrophysics Source Code Library, ascl:2009.003  
 Ineson J., Croston J. H., Hardcastle M. J., Kraft R. P., Evans D. A., Jarvis M., 2015, *MNRAS*, 453, 2682  
 Ineson J., Croston J. H., Hardcastle M. J., Mingo B., 2017, *MNRAS*, 467, 1586  
 Jaffe W. J., Perola G. C., 1973, *A&A*, 26, 423  
 Jarvis M. et al., 2016, MeerKAT Science: On the Pathway to the SKA. p. 6  
 Jonas J., MeerKAT Team, 2016, in MeerKAT Science: On the Pathway to the SKA. p. 1  
 Kempner J. C., Sarazin C. L., 2001, *ApJ*, 548, 639  
 Knobel C. et al., 2012, *ApJ*, 753, 121

- Komberg B. V., Pashchenko I. N., 2009, *Astron. Reports*, 53, 1086
- Laing R. A., Bridle A. H., Parma P., Feretti L., Giovannini G., Murgia M., Perley R. A., 2008, *MNRAS*, 386, 657
- Mack K. H., Klein U., O’Dea C. P., Willis A. G., Saripalli L., 1998, *A&A*, 329, 431
- Mahatma V. H., Hardcastle M. J., Croston J. H., Harwood J., Ineson J., Moldon J., 2019, *MNRAS*, 491, 5015
- Mahatma V. H., Hardcastle M. J., Croston J. H., Harwood J., Ineson J., Moldon J., 2020, *MNRAS*, 491, 5015
- Malarecki J. M., Jones D. H., Saripalli L., Staveley-Smith L., Subrahmanyan R., 2015, *MNRAS*, 449, 955
- Malarecki J. M., Staveley-Smith L., Saripalli L., Subrahmanyan R., Jones D. H., Duffy A. R., Rioja M., 2013, *MNRAS*, 432, 200
- Mohan N., Rafferty D., 2015, *Astrophysics Source Code Library*, ascl:1502.007
- Mostert R. I. J. et al., 2024, *A&A*, 691, A185
- Oei M. S. et al., 2023, *A&A*, 672, A163
- Pandge M. B., Kale R., Dabhade P., Mahato M., Raychaudhury S., 2022, *MNRAS*, 509, 1837
- Pinjarkar S., Hardcastle M. J., Harwood J. J., Lal D. V., Hatfield P. W., Jarvis M. J., Randriamanakoto Z., Whittam I. H., 2023, *MNRAS*, 523, 620
- Planck Collaboration et al., 2016, *A&A*, 594, A13
- Prescott M. et al., 2018, *MNRAS*, 480, 707
- Reiprich T. H., Basu K., Ettori S., Israel H., Lovisari L., Molendi S., Pointecouteau E., Roncarelli M., 2013, *Space Sci. Rev.*, 177, 195
- Safouris V., Subrahmanyan R., Bicknell G. V., Saripalli L., 2008, *MNRAS*, 385, 2117
- Safouris V., Subrahmanyan R., Bicknell G., Saripalli L., 2009, *MNRAS*, 393, 2
- Schneider S. E., Thuan T. X., Magri C., Wadiak J. E., 1990, *ApJS*, 72, 245
- Schoenmakers A., Mack K.-H., De Bruyn A., Röttgering H., Klein U., Van Der Laan H., 2000, *A&ASS*, 146, 293
- Shimwell T. et al., 2022, *A&A*, 659, A1
- Simonte M., Andernach H., Brueggen M., Miley G. K., Barthel P., 2024, *A&A*, 686, A21
- Simonte M., Andernach H., Brüggen M., Schwarz D. J., Prandoni I., Willis A. G., 2022, *MNRAS*, 515, 2032
- Smolčić V. et al., 2017, *A&A*, 602, A1
- Subrahmanyan R., Saripalli L., Hunstead R. W., 1996, *MNRAS*, 279, 257
- Tang H., Scaife A. M. M., Wong O. I., Kapińska A. D., Rudnick L., Shabala S. S., Seymour N., Norris R. P., 2020, *MNRAS*, 499, 68
- Tribble P. C., 1993, *MNRAS*, 261, 57
- Turner R. J., Rogers J. G., Shabala S. S., Krause M. G. H., 2018, *MNRAS*, 473, 4179
- Vardoulaki E. et al., 2015, *A&A*, 574, A4
- Vardoulaki E. et al., 2019, *A&A*, 627, A142
- Wen Z., Han J., Liu F., 2012, *The Astrophysical Journal Supplement Series*, 34, 0067-0049
- Willis A. G., Strom R. G., Wilson A. S., 1974, *Nature*, 250, 625

This paper has been typeset from a  $\text{\TeX}/\text{\LaTeX}$  file prepared by the author.